

Ultrafast response of cubic silicon carbide to intense attosecond pulse lightZehui Liu,¹ Feng Wang ,^{1,*} Xiaowei Sheng,² Jian Wang,³ Lan Jiang,⁴ and Zhiyi Wei⁵¹*School of Physics, Beijing Institute of Technology, Beijing 100081, China*²*Department of Physics, Anhui Normal University, Anhui, Wuhu 241000, China*³*School of Science, Huzhou University, Zhejiang 100083, China*⁴*School of Mechanical Engineering, Beijing Institute of Technology, Beijing 100081, China*⁵*Beijing National Laboratory for Condensed Matter Physics, Institute of Physics, Chinese Academy of Sciences, Beijing 100190, China*

(Received 3 November 2020; revised 15 June 2021; accepted 27 July 2021; published 6 August 2021)

In this paper we are motivated to numerically investigate the fundamental strong-field and attosecond response processes in wide band-gap solids, using the first-principle approach based on time-dependent density functional theory, advancing our understanding of fundamental strong-field and attosecond physics in solids. Taking cubic silicon carbide as a concrete example, the influence of pulse parameters on the ultrafast responses is demonstrated, which allows one to gain a useful independent insight into the interaction processes of attosecond light pulses with solids, revealing information currently not accessible by experiment. We also demonstrate control of the charge transfer and dielectric permittivity by intense attosecond pulse light. It is concluded that a single-cycle attosecond pulse light can be used to effectively manipulate the charge transfer and dielectric properties of wide-band gap materials with great potential for ultrafast device applications.

DOI: [10.1103/PhysRevB.104.064103](https://doi.org/10.1103/PhysRevB.104.064103)**I. INTRODUCTION**

The ultrafast motion of electrons in solids generally involves attosecond timescales on their natural timescales. Indeed, only light pulses of a comparable duration can be used to catch up with the pace of the dynamics of electrons, so attosecond light pulses [1–13] can provide unusual functionality for probing, initiating, driving, and controlling the ultrafast electronic dynamics in solids with unprecedented high temporal and spatial resolutions simultaneously, opening up novel venues for both fundamental and applied sciences, such as attosecond time-resolved motion of electrons interactions in semiconductors [14], attosecond time-resolved photoemission in metals [15], the attosecond control of electrons undergoing photoemission from a nanometer-scale metal tip [16], and attosecond control of collective electron motion in plasmas driven by intense light fields [17]. Researchers have employed attosecond transient absorption spectroscopy to consider questions associated with ultrafast dynamic phenomena in atomic systems, such as real-time observation of valence electron motion in ionized krypton atoms [18], sub-cycle AC stark shift of krypton atom [19] and helium atom [20] excited states, and time-resolved autoionization of argon [21]. In the meanwhile, attosecond transient absorption spectroscopy is rarely applied to molecular systems, unless molecular systems are simple, such as hydrogen molecule and nitrogen molecule [22–24]. Following the first synthesis and characterization of attosecond light pulses, there is a tendency to increase their power and to reduce their duration. Currently, with the advent of powerful attosecond light pulse sources,

the problem of studying the interaction of such pulses with matter is particularly relevant. Of particular interest for us was to explore the exciting possibilities that are opened up by the availability of intense attosecond light sources.

Generally speaking, the interaction of attosecond light pulses with solids can take place in various forms depending heavily on various parameters characterizing the solid system under study and the waveform of attosecond light. It has long been realized that intense light fields can induce extremely nonlinear electronic and optical behaviors in solids [25] which no longer scales linearly with the intensity of the light source, known as various conventional and less conventional strong-field effects, such as Franz-Keldysh effect [26], Bloch oscillations [27], the generation of high-order harmonics in a solid [28,29], the induced electric current in dielectric by intense laser pulses [30], and dynamic metallization in strong optical fields [31]. An important characteristic parameter of attosecond light pulse is the duration of its waveform envelope, which is far less than the characteristic carrier scattering time in solids so that the coherent ultrafast response of pure electronic quantum effects is maintained greatly without interference from detrimental scattering processes. Consequently, it is natural that one might wonder how the crystalline solids respond to the intense attosecond light pulse, and how do the coherence properties of attosecond light pulses transfer into electron wave packets in the crystalline solids accompanied by the constructive and destructive quantum mechanical interference between different quantum pathways due to the quantum physical wave nature of crystal electrons. Currently, there is no measurement technique that would reveal all the details of attosecond strong-field-driven electron dynamics in the crystalline solids, though some time-resolved measurement techniques [32] do provide indirect access to this information.

*wangfeng01@tsinghua.org.cn

Interestingly enough, on account of the ultrashort duration of attosecond light pulses, its interaction with matter is distinguished from conventional long light pulses by a combination of characteristics: (i) One and the same electron state in matter encounters all photons contained in an attosecond light pulse at the same time, enabling therefore interferences between pathways involving different intermediate states that are sensitive to the phase between these photons. (ii) A wide spectral band of photons contained in an attosecond light pulse offers new possibilities to have interferences between more quantum channels, promising a much higher degree of attainable control of electron states in matter. (iii) For high energetic photons contained in an attosecond light pulse, deeper electron states in matter become accessible and electron correlation and multi-electron dynamics becomes increasingly important, leading to the excitation of multiple electrons with a single photon. (iv) Attosecond light pulse gives a direct way to controlling the position and momentum of electrons in speed matched to the electronic timescale.

In addition, as is well known, it is the electronic state that determines all optical properties of a solid media. The electron dynamics need to be controlled with unprecedented accuracy and time resolution to optimize optical responses of the solid media for applications such as ultrafast devices. A quantitative understanding at the cutting-edge, first-principles theoretical level of how electron dynamics proceed in completely new regimes of intense attosecond pulse light parameters, and in particular of the role of the intense attosecond pulse light, will be critical for such optimization, forming the basis for an ultrafast information processing device. However, obtaining a thorough understanding of, and achieving control over, interaction processes of attosecond light pulses with solid media, remains in its infancy.

Intense and ultrashort light pulses are ideal tools to explore ultrafast response of dielectric as their electric fields couple directly to the electrons. The attosecond laser pulses allow us to explore the structure of matter with unprecedented precision, analyze the physics dynamic process of electronic characteristics in atoms, molecules, and condensed states, and even directly manipulate electronic motion. When exposed to an ultrashort few-cycle pulse whose duration is less than the electron relaxation time, the dielectrics can withstand an electric field close to its critical field strength without physical damage. Among the few-cycle pulses, a single-cycle laser pulse provides the best circumstance for studying strong-field effects. Up to now, a single-cycle attosecond waveform has been experimentally realized [2]. The confinement of laser-matter interaction to a single wave cycle will permit accurate experiments of theories of ultrafast response of material under the strong field [3]. The single-cycle attosecond light pulses provide a unique method to control the energy transfer of optical materials in real time on the atomic scale by maximizing recollision energies and suppressing multiple recollision and related undesirable interference effects [33]. Based on these achievements, we here investigate theoretically the strong-field processes in cubic silicon carbide (3C-SiC) and the response process of 3C-SiC to attosecond pulses, which is extensively used in optoelectronics and the advanced microelectronics. The paper is organized as follows, Sec. II describes in brief the theoretical methods and the simulation

details. The calculated results and discussion are presented in Sec. III. Finally, the conclusion is given in Sec. IV.

II. THEORETICAL METHOD

From a fundamental theoretical point of view, the interaction between laser pulse field and matter is a sophisticated physical process in which electrons, ions, and electromagnetic fields are coupled with each other on both coordinates of time and space. The description in terms of the light-matter interaction process was raised in various theoretical methods that have different spatiotemporal resolutions under different approximations. Among the various methods of describing the interaction between light and bulk materials, the popular method is based on the time-dependent density functional theory (TDDFT). There are two complementary approaches. The first is formulated in the frequency domain, which is mainly applied to the linear response of matter exposed to a weak light field. The second is solved in the time domain, which can as well describe the extremely nonlinear effects in the light-matter interaction under external intense light fields. Due to the complexity of the nonlinear coupling among light electromagnetic fields, electrons, and ions, possible consequences or phenomena have not yet been fully discovered. Generally speaking, the occurrence of the interaction of ultrashort laser pulse with bulk materials strongly depends on the waveform of laser cycles and various parameters of the bulk material following the excitation event, as the ultrafast dynamics is dominated by redistribution of electrons. Often, under different time and space scales, there are different levels of approximation for studying the light-matter interaction. A prominent example is in the case of pulse duration shorter than the characteristic timescale of energy transfer from electrons to ions, such kinds of pulses can excite electrons without affecting other parts of the atomic structure. Based on the specific problem at hand, a hierarchy of theoretical approaches should be considered. At the bottom level, the basic equation of TDDFT, i.e., the time-dependent Kohn-Sham (TDKS) equation, is solved in the time domain [34]. The approach at this level can describe the electron dynamics of bulk materials exposed to light fields. The next level of approximation is the coupling of Maxwell equations with the TDKS equation, which can simulate the propagation effect of pulses in bulk solid media [35], and therefore can describe the phenomenon of light-matter interaction both macroscopically and microscopically. At the third level of approximation, ion or lattice dynamics is introduced through the Ehrenfest molecular dynamics (MD) [36]. Throughout this paper, the Gaussian unit system of electromagnetic fields and atomic units $e = \hbar = m_e = 1$ are used unless stated otherwise.

In this paper we describe electron dynamics in a unit cell of a crystalline solid with the periodic boundary conditions under a time-dependent, spatially uniform vector potential, which is related to the external electric field $\mathbf{E}(t) = -(1/c)\partial\mathbf{A}(t)/\partial t$ where c is the scalar speed of light in vacuum. The effective one-electron equation can be solved in the framework of TDDFT:

$$i\hbar\frac{\partial\psi_i(\mathbf{r},t)}{\partial t} = \hat{H}_{\text{ks}}\psi_i(\mathbf{r},t). \quad (1)$$

\hat{H}_{ks} is the Hamilton defined by

$$\hat{H}_{\text{ks}} = \frac{1}{2m_e} \left[-i\hbar\nabla + \frac{e}{c}\mathbf{A}_{\text{tot}}(\mathbf{r}, t) \right]^2 + V_{\text{tot}}(\mathbf{r}, t), \quad (2)$$

with time-dependent total potentials

$$\mathbf{A}_{\text{tot}}(\mathbf{r}, t) = \mathbf{A}_{\text{ext}}(\mathbf{r}, t) + \mathbf{A}_{\text{ind}}(\mathbf{r}, t), \quad (3)$$

$$\mathbf{A}_{\text{ind}}(t) = \mathbf{A}_{\text{EM}}(t) + \mathbf{A}_{\text{XC}}(t), \quad (4)$$

$$V_{\text{tot}}(\mathbf{r}, t) = V_{\text{ion}}(\mathbf{r}, t) + \int d\mathbf{r}' \frac{e^2 \rho_e(\mathbf{r}', t)}{|\mathbf{r} - \mathbf{r}'|} + V_{\text{XC}}(\mathbf{r}, t), \quad (5)$$

where e is an elementary charge ($e > 0$), m_e is the mass of an elementary charge, and $\rho_e(\mathbf{r}, t) = 2\sum_i |\psi_i(\mathbf{r}, t)|^2$ is the valence electron number density with the index i running over the occupied one-electron orbitals ψ_i which are spin distinguished, the factor of 2 indicates that each orbital is fully occupied. A time-dependent Bloch wave function $\psi_i(\mathbf{r}, t) = e^{i\mathbf{k}\cdot\mathbf{r}} u_{n\mathbf{k}}(\mathbf{r}, t)$ is introduced since the Hamiltonian \hat{H}_{ks} in Eq. (1) has the same lattice periodicity at each time, n is the band index, the other index \mathbf{k} of the orbitals is the crystalline momentum which is discretized in the first Brillouin zone. The time evolution of the Bloch wave functions is calculated in practice. $V_{\text{ion}}(\mathbf{r}, t)$ denotes the interaction of valence electron and ionic cores described by a norm-conserving pseudopotentials [37], and $V_{\text{XC}}(\mathbf{r}, t)$ is the exchange-correlation (XC) potential in the adiabatic approximation.

The induced potential $\mathbf{A}_{\text{ind}}(t)$ originates from the surface charging effect which corresponds to the longitudinal geometry [34,38–40]. The induced field is composed of the full electromagnetic potential $\mathbf{A}_{\text{EM}}(t)$ and that of the macroscopic exchange-correlation field $\mathbf{A}_{\text{XC}}(t)$, as introduced in Eq. (4) [41]. We choose the Weyl gauge condition. It should be noted that the macroscopic components of the exchange-correlation contribution will not be considered in our study. The full electromagnetic potential $\mathbf{A}_{\text{EM}}(\mathbf{r}, t)$ satisfies the following equation [42]:

$$\left(\nabla^2 - \frac{1}{c^2} \frac{\partial^2}{\partial t^2} \right) \mathbf{A}_{\text{EM}}(\mathbf{r}, t) - \nabla[\nabla \cdot \mathbf{A}_{\text{EM}}(\mathbf{r}, t)] = -\frac{4\pi}{c} \mathbf{j}(\mathbf{r}, t), \quad (6)$$

$\mathbf{j}(\mathbf{r}, t)$ is the electric current density which can be written as

$$\mathbf{j}(\mathbf{r}, t) = -2e \sum_i \text{Re}[\psi_i^*(\mathbf{r}, t) \hat{\mathbf{v}} \psi_i(\mathbf{r}, t)], \quad (7)$$

with $\hat{\mathbf{v}}$ the velocity operator [43,44]

$$\hat{\mathbf{v}} = \frac{1}{i\hbar} [\hat{\mathbf{r}}, \hat{H}_{\text{ks}}]. \quad (8)$$

In the microscopic scale of the unit cell, an approximation of a coarse graining by neglecting the spatial variation is applied. The $\mathbf{A}_{\text{EM}}(t)$ satisfies

$$\frac{d^2 \mathbf{A}_{\text{EM}}(t)}{dt^2} = 4\pi c \mathbf{J}(t), \quad (9)$$

where $\mathbf{J}(t)$ is taken as an average of $\mathbf{j}(\mathbf{r}, t)$ over the unit cell.

In this paper we follow the pump-probe experiment to investigate the laser-matter interaction. The electron dynamics under a spatially uniform, time-dependent vector potential

field is taken into account. The specific waveform [38] of the pump pulse laser are described using the following equation:

$$\mathbf{E}(t) = \mathbf{E}_0 e^{-(t/\tau)^2} \left(1 - \frac{2t^2}{\tau^2} \right), \quad (10)$$

where \mathbf{E}_0 and τ are the amplitude and duration with the corresponding central frequency $\omega_0 = 2\hbar/\tau$. It is worth noting that for ultrashort single-cycle pulses, the real center frequency will deviate. In atomic units (or, more precisely, in any Gaussian system of units), the relationship between peak electric field and peak intensity is $\mathbf{I}_0 = \frac{c}{8\pi} \mathbf{E}_0^2$. In the actual simulation, the laser peak intensity mentioned refers to the intensity of the laser peak electric field inside the medium. The full pump pulse duration is defined as 6τ . The wavelength is much longer than the size of the unit cell. The single-cycle laser pulse is powerful enough to drive strong-field processes. The probe laser having a step function envelope can be written in the form [34]

$$\mathbf{A}(t) = \mathbf{A}_0 \theta(t - t_0), \quad (11)$$

where \mathbf{A}_0 is the amplitude and t_0 is a certain instant of time. According to the response of 3C-SiC to the probe laser, one can extract the dielectric permittivity. The dynamic dielectric permittivity $\varepsilon_{m,m}(\omega)$ (for the case of $m = n$) is defined as [38,44,45]

$$\varepsilon_{m,m}(\omega) = \frac{\mathbf{E}_{\text{ext},m}(\omega)}{\mathbf{E}_{\text{tot},m}(\omega)}, \quad (12)$$

where the terms $\mathbf{E}_{\text{ext},m}(\omega)$ and $\mathbf{E}_{\text{tot},m}(\omega)$ are external electric field and total electric field of probe laser, respectively, m and n indicate Cartesian component ($m, n = x, y, z$).

In the actual simulation there are two calculations that have to be done, pump-only and pump-probe calculation once. Then subtract ‘‘pump’’ influence on the induced component, leaving the response part of the system to ‘‘probe’’ only. The actual procedure can be expressed as

$$\frac{d\mathbf{A}_{\text{ind}}^{\text{probe}}(t)}{dt} = \frac{d\mathbf{A}_{\text{ind}}^{\text{pump+probe}}(t)}{dt} - \frac{d\mathbf{A}_{\text{ind}}^{\text{pump}}(t)}{dt}. \quad (13)$$

It is noteworthy that the spatially uniform, time-dependent vector potential is related to the electric field by $\mathbf{A}(t) = -c \int_{-\infty}^t dt' \mathbf{E}(t')$. Therefore, Eq. (12) can be written with the Fourier transform at frequency ω :

$$\frac{1}{\varepsilon_{m,m}(\omega)} = \frac{\int dt e^{i\omega t} \mathbf{E}_{\text{tot},m}^{\text{probe}}(t)}{\int dt e^{i\omega t} \mathbf{E}_{\text{ext},m}^{\text{probe}}(t)} = 1 + \frac{\int dt e^{i\omega t} \frac{d\mathbf{A}_{\text{ind},m}^{\text{probe}}(t)}{dt}}{\int dt e^{i\omega t} \frac{d\mathbf{A}_{\text{ext},m}^{\text{probe}}(t)}{dt}}. \quad (14)$$

The snapshot of the dielectric permittivity of the system at a certain time t_0 is determined by the formula

$$\frac{1}{\varepsilon_{m,m}(\omega)} = 1 + \frac{1}{\mathbf{A}_{0,m}} \int_{t_0}^{T_{\text{probe}}} dt e^{i\omega t - \gamma t} \frac{d\mathbf{A}_{\text{ind},m}^{\text{probe}}(t)}{dt}, \quad (15)$$

where γ is a damping factor, in numerical sense, γ can be used as a smearing parameter to simulate finite lifetime effects of the excitations. Thus, the peaks in the absorption spectrum obtain a limited width. The integration over time T_{probe} is over full probe laser duration. In the present work our simulations are partly carried out with OCTOPUS code (version

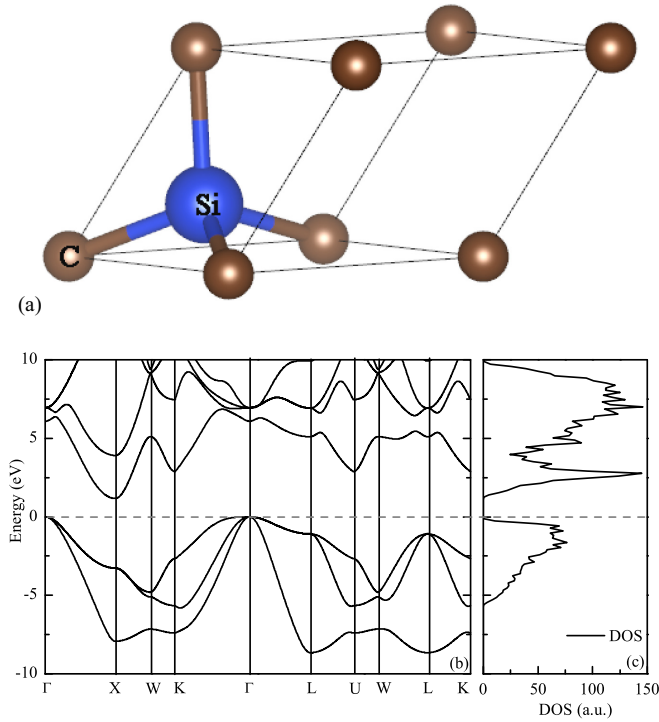


FIG. 1. (a) The three-dimensional structure of 3C-SiC. (b) The electronic band structure of 3C-SiC. (c) The electronic density of the state of 3C-SiC.

8.3) [46–48], which is a scientific program package specially designed to solve DFT and TDDFT problems.

III. RESULTS AND DISCUSSION

The wide band-gap semiconductor 3C-SiC has superior characteristics, such as stable structures, high electron mobility, saturated electron drift velocity, high corrosion resistance, favorable chemical inertness, and small neutron absorption cross section [49–53]. It will be very interesting to know the ultrafast response mechanism in 3C-SiC under an ultrashort single-cycle laser pulse irradiation. 3C-SiC belongs to face-centered cubic lattice, its primitive unit cell including one Si atom and one C atom with lattice parameter $a = 5.85$ a.u., is shown in Fig. 1(a). The electronic band structure and density of states (DOS) are shown in Figs. 1(b) and 1(c). The calculation used a k -point mesh of $18 \times 18 \times 18$, along with the Perdew-Burke-Ernzerhof (PBE-GGA) [54] exchange and correlation functional. The energy gap is 1.3 eV, corresponding well to the result on the AFLOW website [55].

Figure 2 shows the real and imaginary parts of the dielectric permittivity of 3C-SiC in ground state. We display the dielectric permittivity calculated by two kinds of code. The codes are ELK and OCTOPUS, respectively. The ELK code and OCTOPUS code calculate the dielectric permittivity in different approaches [44,56]. In fact, we did a comparison between the two approaches. The overall trend of the dielectric permittivity calculated by these two codes is consistent, as shown in Fig. 2. Obviously the results obtained from ELK code are more consistent with the experimental values (Fig. 2, circles) [57] in details, which is expected, due to the approach of calculating

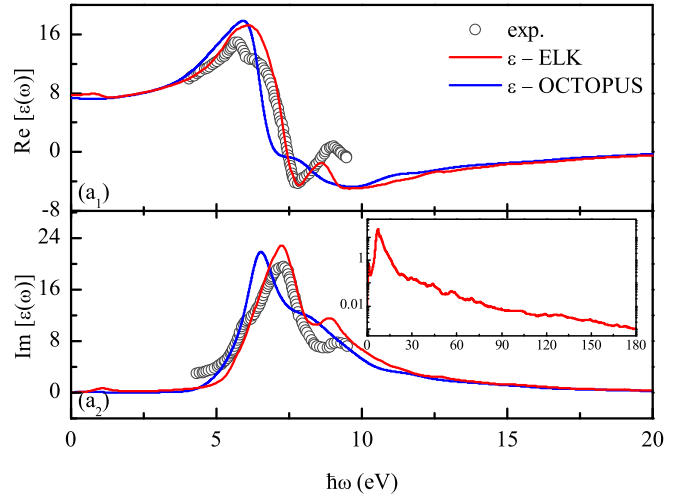


FIG. 2. The real (upper panel) and imaginary parts (bottom panel) of the dielectric permittivity of ground state 3C-SiC. The inset is the imaginary part of the dielectric permittivity of the larger photon energy range. Red lines: The dielectric permittivity obtained by ELK code. Blue lines: The dielectric permittivity calculated by OCTOPUS code.

the dielectric permittivity of ELK code is more accurate than that of OCTOPUS code. In fact, we present the results obtained by the two codes to compare and check the validity of the theoretical method. The calculation details for OCTOPUS code are as follows. The effective one-electron equation is solved in real time and real space. The orbital wave functions ψ_i are represented on a three-dimensional mesh of $20 \times 20 \times 20$ grid points with spacing of 0.4 a.u. The number of k points in the Brillouin zone is taken as $16 \times 16 \times 16$. The real-time propagation is performed with the enforced time reversal symmetry method [58] with a time step of 0.02 a.u. We have carefully examined the convergence of the results with respect to these parameters. The PBE-GGA functional is chosen here. In order to ensure the spectrum obtained through the Fourier transform has sufficient resolution, the time period T_{probe} of the probe laser used in our calculation is set to 200 a.u. A proper damping factor $\gamma = 0.015$ is chosen for the subsequent study. Our calculations are in good agreement with the experimental values. At around 6 eV the dielectric permittivity of 3C-SiC shows a distinct shoulder which is related to the lowest direct interband transition.

In the following we will explore the safe parameter range for the energy absorption of each atom in 3C-SiC, i.e., the average energy absorbed by each atom which does not reach the damage threshold. The laser-material energy absorption per unit cell volume of Ω can be defined by the difference between the electronic energy at an instant time t and at the ground state in the simulation. The absorbed energy is also equivalent to the work done by the applied external pump electric field $\mathbf{E}(t)$, determined by

$$W(t) = \Omega \int_{-\infty}^t dt' \mathbf{E}(t') \cdot \mathbf{J}(t'). \quad (16)$$

The damage threshold can be estimated by the critical criterion of energy or density [39,59], here the energy critical

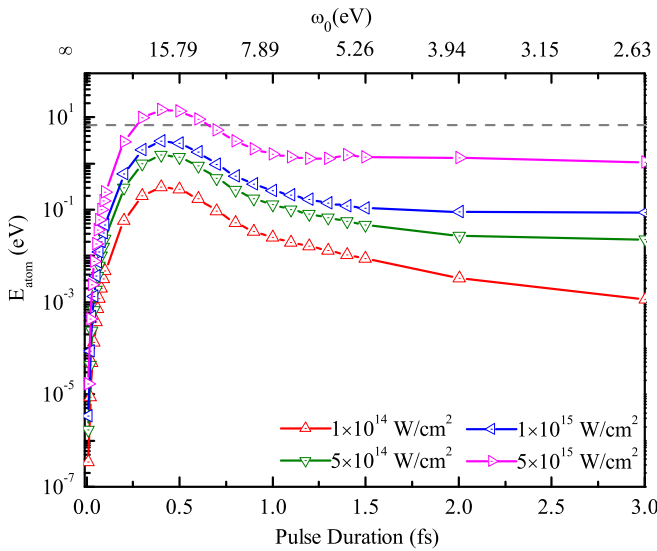


FIG. 3. The energy absorption of each atom in 3C-SiC crystal with various laser intensities and pulse durations is calculated. The single-cycle pulse is expressed as the Eq. (10). The top axis corresponds to the central frequency $\omega_0 = 2\hbar/\tau$ of each laser pulse.

standard is adopted. The energy standard we adopted here will correspond to the vaporization of the material. The horizontal gray solid line in Fig. 3 denotes the average cohesive energy value 6.84 eV of per atom of 3C-SiC calculated by ELK code [60]. The experimental value is 6.34 eV obtained from Jiang *et al.* [61]. The energy absorption of each atom is defined as $E_{\text{atom}} = \lim_{t \rightarrow \infty} W(t)/n_{\text{atom}}$, where n_{atom} is the total number of atoms in the unit cell. One expects an ultrashort laser pulse would lead to fascinating physical phenomena. We use a single-cycle laser waveform expressed as Eq. (10) to simulate a single-cycle ultrashort pulse laser. Figure 3 shows how the pulse peak intensity and duration influence the electron dynamics. Inspecting Fig. 3, one finds that the average energy absorbed by each atom of 3C-SiC exceeds the cohesive energy value when the laser has peak intensity $I = 5 \times 10^{15} \text{ W/cm}^2$ and full pulse duration $T = 0.4\text{-}0.6 \text{ fs}$. Particularly, one finds a relatively large region of parameters allowing for zero damage. At longer pulse duration, the safe parameters depend on the intensity rather than pulse duration. Besides, one can figure out how the absorption rate depends on pulse duration and central frequency, as shown in Fig. 4. The total energy of laser pulse can be estimated by $\sum \propto \int \frac{c}{8\pi} E^2(t) dt$, therefore, the absorption rate can be given by $A_{\text{abs}} \propto E_{\text{atom}}/\sum$. Obviously the absorption rate shows a peak position at $T = 0.45 \text{ fs}$, which is consistent with the peak position in Fig. 3.

Figure 5 further displays a series of energy transfer with a variety of full pulse duration T from a single-cycle ultrashort pulse laser to 3C-SiC crystal, which is helpful to analyze the dependence of energy transfer on ultrashort pulse laser intensity. When the full pulse duration is $T \leq 2 \text{ fs}$, E_{atom} curves are linear with respect to increasing peak laser intensity, and the E_{atom} curves are parallel to each other. When the full pulse duration is $T \geq 2.9 \text{ fs}$, the E_{atom} curves are no longer parallel to the energy absorption curves above and change substantially.

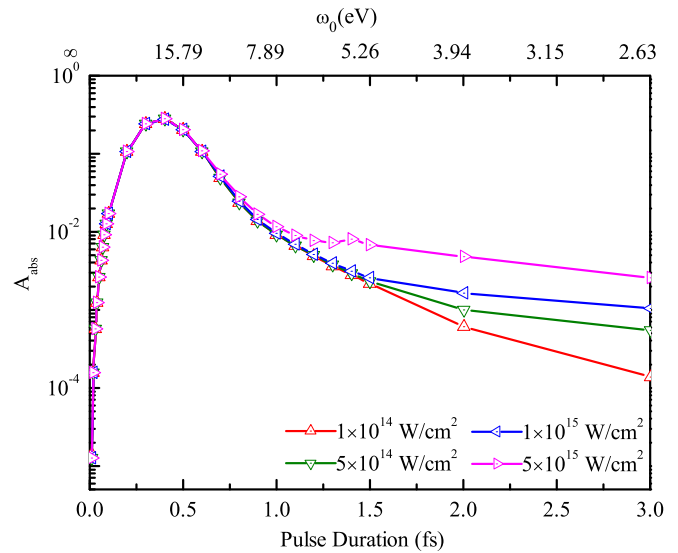


FIG. 4. The energy absorption rate of each atom in 3C-SiC crystal with various laser intensities and pulse durations is calculated. The single-cycle pulse is expressed as Eq. (10). The top axis corresponds to the central frequency $\omega_0 = 2\hbar/\tau$ of each laser pulse.

By comparing the energy transfer shown in Figs. 3 and 5, it is found that $W(t)$ always keeps the maximum value at $T = 0.45 \text{ fs}$. To explain the maximum energy absorption appearing in Figs. 3 and 5, we illustrate the time-dependent energy transfer $W(t)$, electric current density $j(t)$, and charge transfer $Q(t)$ with various attosecond pulse duration in Fig. 6, which is compared with that under femtosecond laser pulse (for the case of 2.9 fs). The curve of the external laser field is added to each panel (gray solid line) for the phase comparison. Taking the case of $I_1 = 1 \times 10^{15} \text{ W/cm}^2$ as an example, we can observe that $W(t)$ increases synchronously with the laser field until the pulse reaches its peak intensity. However, when $T = 0.1$ and 2.9 fs, an obvious reverse energy flow is observed at the trailing edge of the laser field, especially at $T = 2.9 \text{ fs}$,

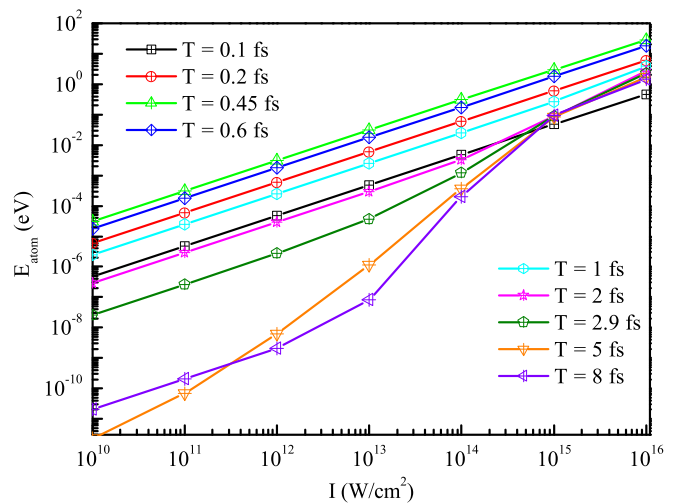


FIG. 5. The energy absorption of each atom in 3C-SiC crystal as a function of laser peak intensities I . The single-cycle pulse is expressed as Eq. (10).

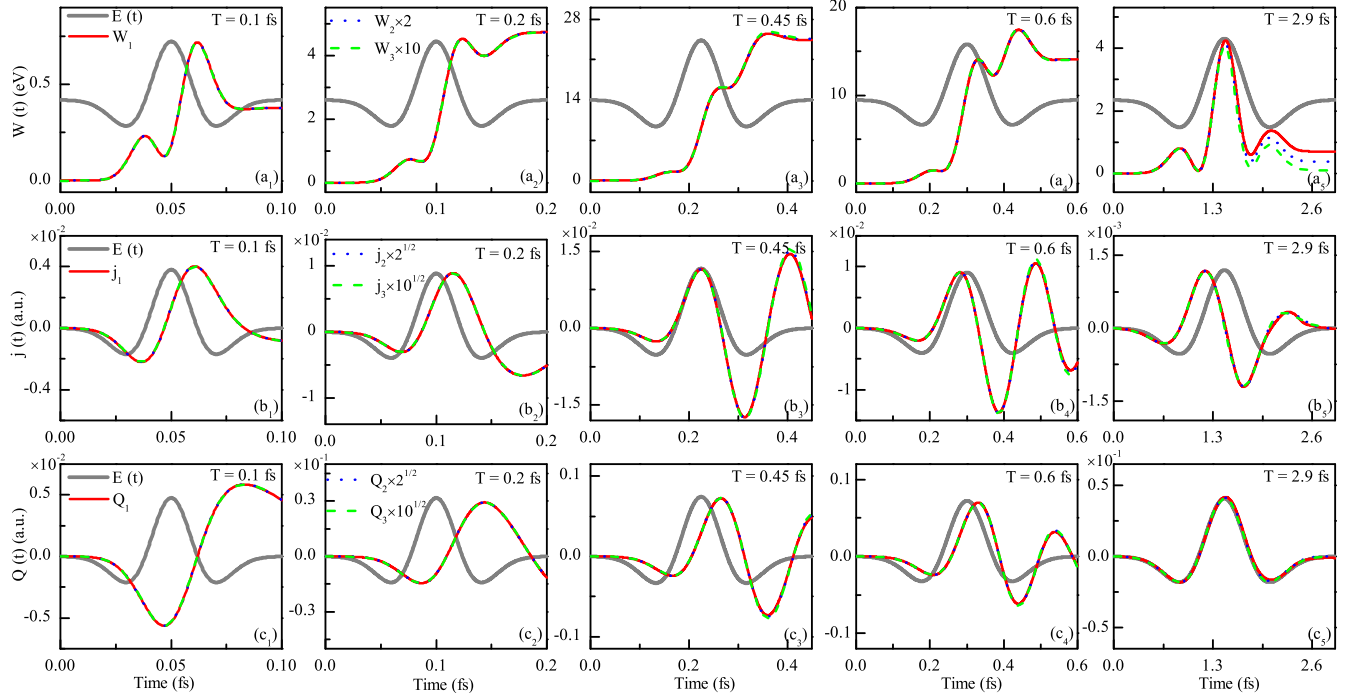


FIG. 6. (a₁)–(a₅) The time-dependent energy absorption $W(t)$ in 3C-SiC crystal pumped by single-cycle laser pulses with $I_1 = 1 \times 10^{15}$ W/cm² (red solid line), $I_2 = 5 \times 10^{14}$ W/cm² (blue dotted line), and $I_3 = 1 \times 10^{14}$ W/cm² (green dashed line). (b₁)–(b₅) The calculated electric current density $j(t)$ with laser parameters corresponding to (a₁)–(a₅). (c₁)–(c₅) The transferred charge $Q(t)$ with laser parameters corresponding to (a₁)–(a₅). The gray solid line denotes the applied laser field.

which is an inherent result of some of the energy being transferred back to the radiation field. The periodic excitation and deexcitation in Figs. 6(a₁)–6(a₂) are mainly due to the interaction of virtual excitation [62] as they largely represent distortions of initial electronic states. Figures 6(a₁)–6(a₅) show that $W(t)$ obtained under different peak laser intensities are completely coincident after being multiplied by a certain scale factor [for the case of $I_3 = 1 \times 10^{14}$ W/cm² $W(t)$ is multiplied by 10 and for the case of $I_2 = 5 \times 10^{14}$ W/cm² $W(t)$ is multiplied by 2].

Three types of dynamic response in and out of resonance in electric current are observed. Figures 6(b₁)–6(b₂) display a positive detuning from the resonance, Fig. 6(b₃) shows a resonant excitation profile, and Figs. 6(b₄) and 6(b₅) show negative detuning from the resonance, respectively. Figures 6(b₁), 6(b₂), and 6(b₅) indicates that $j(t)$ shows a significant $\pi/2$ phase shift relative to the laser pulse at peak time. This indicates that a nondissipative response has occurred. Figure 6(b₃) denotes that when $T = 0.45$ fs, the phase of $j(t)$ coincides with the phase of the drive pulse at peak time. Because resonance occurs between the frequency of the external laser field and the natural frequency of the material. Figures 6(b₁)–6(b₅) display that $j(t)$ calculated with various intensities is exactly matched with each other after being multiplied by a certain scale factor [for the case of $I_3 = 1 \times 10^{14}$ W/cm² $j(t)$ is multiplied by $\sqrt{10}$ and for the case of $I_2 = 5 \times 10^{14}$ W/cm² $j(t)$ is multiplied by $\sqrt{2}$]. The electron dynamics in an intense optical pulse field shows high frequency Bloch oscillations, which is visible in the calculated electric current density $j(t)$, corresponding to strong modification of intraband electron dynamics.

The charge transfer $Q(t)$ along the laser polarization are shown in Figs. 6(c₁)–6(c₅) together with the electric field of the laser pulse. The transferred charge is one of the characteristics of light-matter interaction, which is calculated from $Q(t) = \Omega \int_{-\infty}^t j(t') dt'$. The calculated $Q(t)$ with various intensities exactly matches with each other after being multiplied by a certain scale factor [for the case of $I_3 = 1 \times 10^{14}$ W/cm² $Q(t)$ is multiplied by $\sqrt{10}$ and for the case of $I_2 = 5 \times 10^{14}$ W/cm² $Q(t)$ is multiplied by $\sqrt{2}$]. Meanwhile, the transferred charge $Q(t)$ is related to the direction of the pulse-field maximum, and $Q(t)$ gradually conforms to the electric field curve with the increase of pulse duration. The pulse-field maximum is positive, pointing in the positive direction of the z axis. An interesting property of the transferred charge is the change of its sign with increasing pulse duration. While at small pulse duration 0.1, 0.2, and 0.45 fs, the total transferred charge is positive, namely, the charge is transferred in the direction coincident to the direction of the pulse-field maximum, at large pulse duration 0.6 and 2.9 fs, the total transferred charge is negative, the charge is transferred in the direction opposite to the direction of the pulse-field maximum. For dielectrics, the total transferred charge is positive, while for metals, the total transferred charge is negative [63]. The system excited by small pulse duration shows a dielectric response, the system excited by large pulse duration shows a metal response. This is consistent with the change in the dielectric permittivity as shown in Fig. 12 below. The most interesting result of combining excitation and laser-driven motion is that this may result in a nonzero charge $Q(t)$ transferred by a laser pulse, which represents finite interband transitions. The finite interband transitions

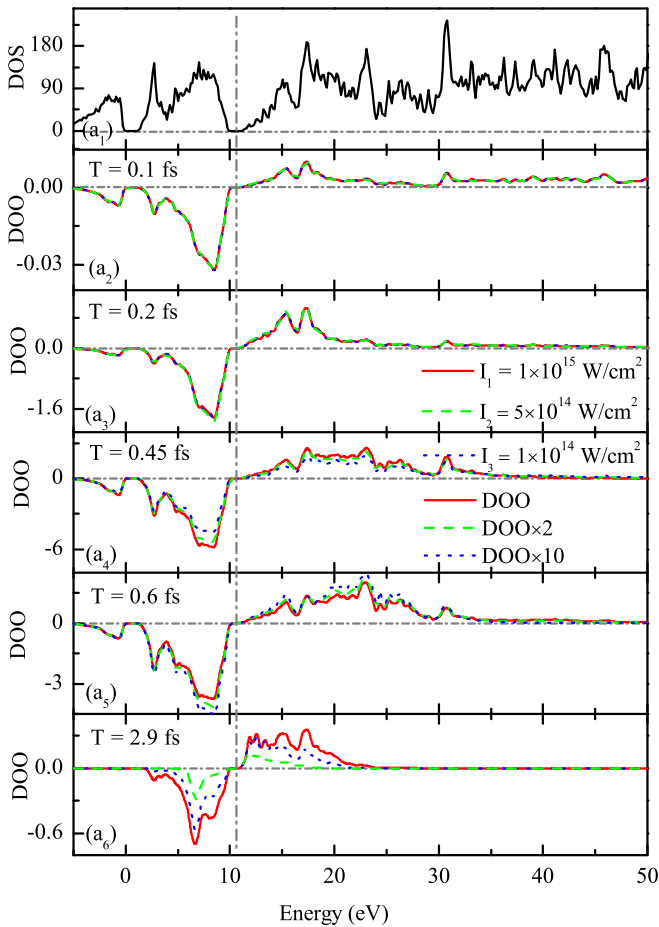


FIG. 7. (a₁) The calculated electronic density of the state of 3C-SiC. (a₂)–(a₆) The difference of occupation (DOO) number between the ground state and the excited state after the laser pulse.

would lead to a finite residual polarization of the electron system.

In this part we shortly highlight the mechanism of optical and electric control methodologies to ultrashort laser control of ultrafast processes with an emphasis on processing of dielectrics on the femtosecond and attosecond scale. We examine in more detail the distribution of electrons and holes in the excitation. Figure 7(a₁) shows the calculated static electronic density of the state in 3C-SiC as a function of energy. The calculation of DOO is performed by real-time propagation of the electron occupation number, as implemented in the SALMON code [64,65]. DOO means the difference of occupation number between the ground state and the excited state after the laser pulse ends. The number of k points in the Brillouin zone is taken as $12 \times 12 \times 12$. The grid spacing of the Cartesian coordinate system is set to $16 \times 16 \times 16$. The calculation in SALMON uses the same XC potential PBE-GGA and laser wave packet as OCTOPUS. The vertical dashed line represents the Fermi level. This is clearly visible in Figs. 7(a₂)–7(a₆), where the distribution in the final state for the three pulse intensities is shown by red solid lines ($I_1 = 1 \times 10^{15} \text{ W/cm}^2$), green dashed lines ($I_2 = 5 \times 10^{14} \text{ W/cm}^2$), and blue dotted lines ($I_3 = 1 \times 10^{14} \text{ W/cm}^2$). With the increase of the full pulse duration from

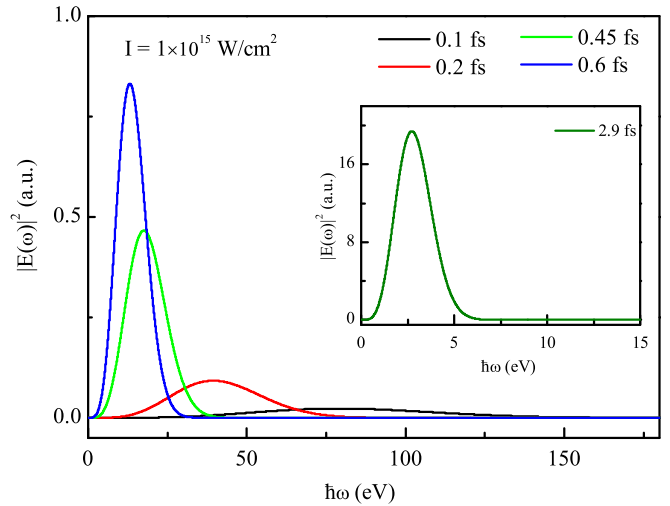


FIG. 8. The photon number density distribution $|E(\omega)|^2$ of laser pulses with different durations at the same laser peak intensity $I = 1 \times 10^{15} \text{ W/cm}^2$ expressed as Eq. (10).

0.1 to 2.9 fs (for five frequencies beyond the gap as shown in Fig. 8), the variation range of DOO on the horizontal axis becomes narrower. Because the monochromaticity of the laser becomes stronger with the increase of full pulse duration. One can see a progression of distributions with the full pulse duration 0.45 fs exciting much deeper levels than the other pulses. This agrees with the increase in the real part of the dielectric permittivity, as shown in Fig. 12. The reason is that the laser frequency is consistent with the intrinsic frequency of 3C-SiC, the material absorbs the more energy and the dielectric permittivity changes more dramatically, as shown in Figs. 5 and 12. This implies that the determination of the distribution of electrons and holes is particularly suitable for explanation of ultrafast responses of ultrashort pulses and the character of the distribution does not depend strongly on the pulse intensity. Figures 7(a₂)–7(a₃) show that DOOs obtained under different peak laser intensities are completely coincident after being multiplied by a certain scale factor (for the case of $I_3 = 1 \times 10^{14} \text{ W/cm}^2$ DOO is multiplied by 10 and for the case of $I_2 = 5 \times 10^{14} \text{ W/cm}^2$ DOO is multiplied by 2), while DOOs are not coincident with each other after being multiplied by a certain scale factor when the laser pulse becomes longer. This implies that the linear phenomenon is more obvious at the attosecond scale. The linear dependence of DOO on the peak intensity of the attosecond pulse is fully justified, because even with a very intense attosecond pulse light, the photon number density at each frequency involved in such a pulse is not a large value due to its broadband spectra, as seen in Fig. 8. The absorption energy of the interaction between ultrashort attosecond pulses and matter and the linear increase of DOO with the peak laser intensities of the pulses come from the fact that the photon number density of the attosecond pulse is less than that of a long pulse with the same peak laser intensities. On the one hand, because the photon number density of each frequency contained in the attosecond pulse is very small, the interaction between attosecond pulse light and matter shows the single-photon linear response behavior with the pulse intensity below 10^{16} W/cm^2 . On the

other hand, because the attosecond light pulse has a wide spectral band of photons, different combinations of quantum pathway can have dynamical interferences [66,67]. The final occupation number of electron states is determined by the dynamic interference of the different quantum pathways. The dynamic interference can be constructive or destructive. By introducing dynamical interferences, it is possible to alter the classical linear response behavior, for example, the dark light pulse which have the same spectral content as a conventional pulse but are not absorbed by conventional absorbing media as an extreme case. Hence, we refer to this new effect as the linear dynamic interference response mechanism, in order to be different from the traditional linear response mechanism.

To discuss the above points further, we show $|E(\omega)|^2 = |\int dt E(t)e^{i\omega t}|^2$ in Fig. 8, which is proportional to the photon number density $N_{\text{photon}}(\omega) = \frac{c}{2\pi} |E(\omega)|^2 / \hbar\omega$. For the purposes of this study it is important to emphasize that the shorter the pulse duration, the wider the photon band, and the less the photon number density of the same frequency. Under the action of the femtosecond laser pulse, 3C-SiC can absorb multiple photons of the same frequency at one time, so the energy absorption curve shows a nonlinear absorption phenomenon. The attosecond pulse consists of a wide energy range of photons, the absorbed energy is the average of the single-photon absorption processes for different frequencies, thus it illustrates a linear phenomenon as shown in Fig. 5. This kind of behavior is clearly different from multiphoton absorption behavior under the action of the traditional long-pulsed strong field in which electrons absorb multiple photons of the same frequency at the same time. In short, although the peak laser intensities of the attosecond pulses in the time domain can be very intense, the photon number density of each frequency contained in the frequency domain is not large, which is the reason why the interaction between attosecond pulses and matter exhibits linear characteristics in energy absorption and DOO map.

From a linear response point of view, the absorbed energy can be expressed as

$$A_{\text{LR}}(t) \propto \int |E(\omega)|^2 \omega \text{Im}\varepsilon(\omega) d\omega, \quad (17)$$

where the $\text{Im}\varepsilon(\omega)$ is the imaginary part of the dielectric permittivity of ground state 3C-SiC. A comparison of the results of our computational simulation with those of the linear absorption equation is shown in Fig. 9. The deviation between our computational simulation and linear absorption equation indicates that there is indeed an uncommon absorption behavior when 3C-SiC interacts with attosecond pulses, which corresponds to the linear dynamic interference response mechanism. It should be noted that we consider attosecond-long laser pulses, for which the duration of the pulse is less than the electron scattering time. For such a short pulse, the electron dynamics is coherent. The broadening of photon spectral band promises a much higher degree of attainable quantum interference effects because all pathways involving different frequency photons become accessible simultaneously, this laid the foundation of lightwave electronics [68] based on attosecond pulses. The uncommon absorption behavior is the result of the interference effect between

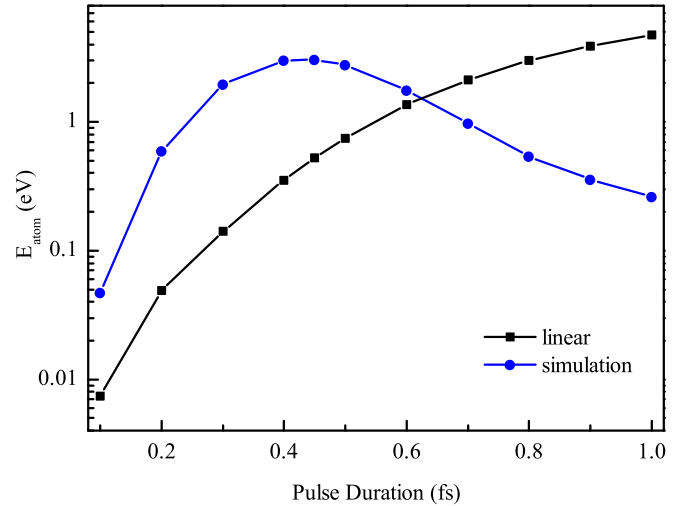


FIG. 9. The energy absorption of each atom in 3C-SiC crystal pumped by single-cycle laser pulses with $I = 1 \times 10^{15}$ W/cm². Blue line: The result of our simulation. Black line: The result of linear absorption equation (17).

various transition channels when attosecond pulse irradiates 3C-SiC.

Another characteristic of electron dynamics in the time-dependent electric field of the laser pulse is the excited electron number between the conduction and valence band. The definition of the excited electron number in this paper is that based on the projections of the time evolved wave functions on the ground state wave functions. The number of excited electrons is shown in Fig. 10 for different pulse durations together with the corresponding electric field of laser pulses (gray solid line). The excited electrons after the pulse ends are large and are sensitive to the pulse durations. Obviously the electron system does not return to its original state after the pulse ends, i.e., the time-dependent excited electrons indicate that the electron dynamics is irreversible. Another feature is the phase shift between the excited electron number and the electric field. The maxima of excited electron number corresponds to the moment when the electric field is zero. The phase shift is due to strong dependence of the interband coupling on the wave vector. Irreversible dynamics of electron system and phase shift persist at all pulse durations as a result of the interband transitions which is consistent with the facts revealed by electrons charge transfer.

The electron density difference on the plane with Miller indices (1 0 0) and $0.75a$ distance from origin through the unit cell is shown in Fig. 11. The electron density difference is defined by the difference between the electron density at an instant time t with respect to the ground state electron density. The particle-hole excitation changes the occupation probabilities in the final state, affecting the electron density distribution. Figures 11(a)–11(d) display the change of electron density in the final state after laser pulses with different pulse duration. There is one special state which corresponds to the case of resonant excitation in Fig. 11(b) where electron density changes most from that in the ground state, the number of excited electrons is also the highest [Fig. 10(b)]. The other three are the positive detuning excitation and negative

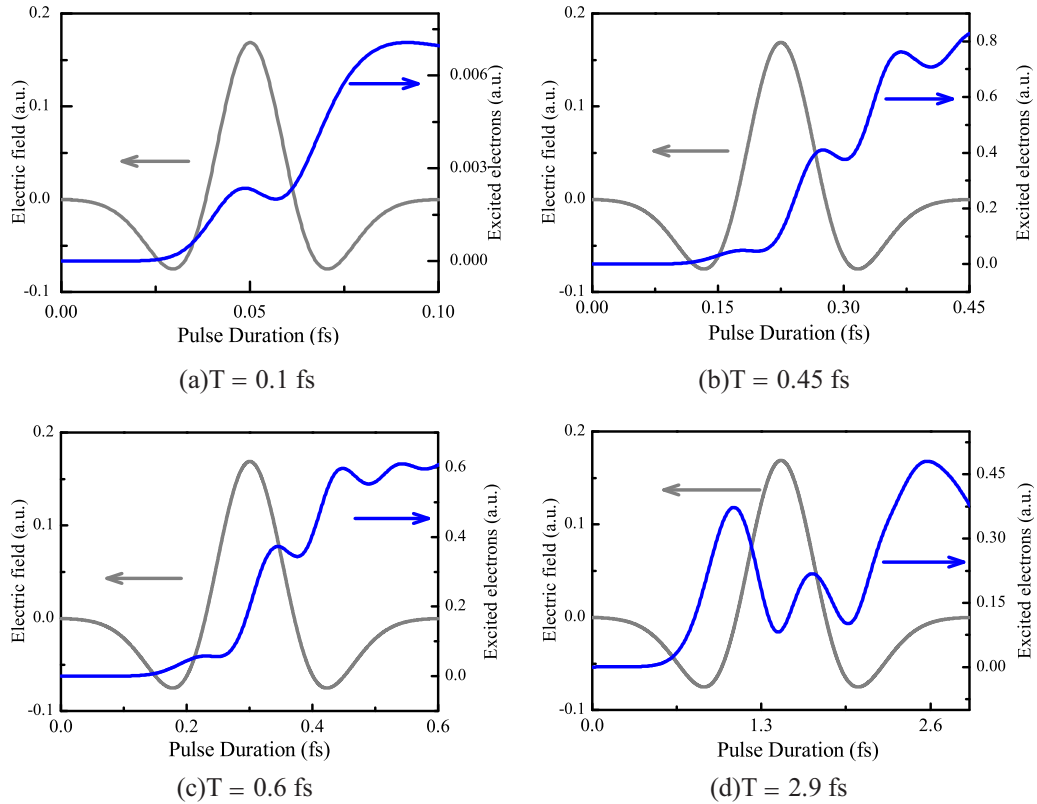


FIG. 10. Time-dependent excited electrons (blue solid lines) and the corresponding time-dependent electric field of the laser pulse (gray solid lines) at the peak laser intensity $I = 1 \times 10^{15}$ W/cm² are shown. The polarization of the pulse is along axis z .

detuning excitation from the resonance as shown in Figs. 11(a), 11(c), and 11(d), respectively. The effect is much bigger in Fig. 11(b) because the difference of occupation number between the ground state and the excited state after

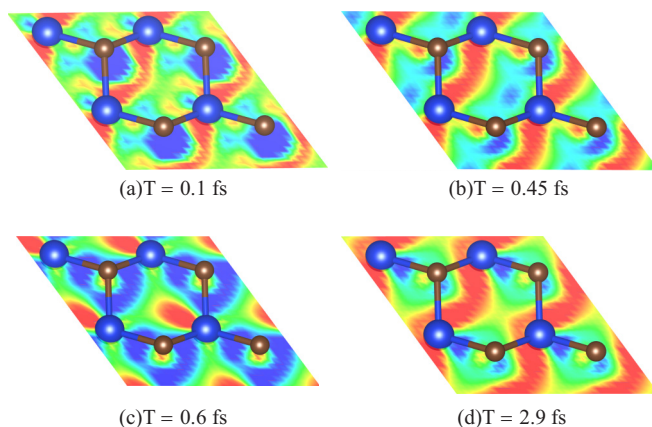


FIG. 11. The electron density difference in the panel cutting through four Si atoms [Miller indices (1 0 0) and the distance from origin is $0.75a$]. (a)–(d) Electron density difference in the final state after laser pulses with different pulse duration at the peak laser intensity $I = 1 \times 10^{15}$ W/cm². The color represents a positive (red) or negative (blue) electron density difference around the ionic cores, saturation level ranges (a) from -0.0007 to 0.0007 , (b) from -0.004 to 0.004 , (c) from -0.004 to 0.004 , and (d) from -0.0007 to 0.0007 .

the laser pulse changed more dramatically as illustrated in Fig. 7(a₄).

In order to study the effect of attosecond and femtosecond laser pulses on the dielectric response of 3C-SiC, we calculated the dielectric permittivity of excited 3C-SiC as shown in Fig. 12. The spectra in Fig. 12 show the dielectric permittivity of 3C-SiC excited by single-cycle ultrashort laser pulses with various pulse durations. For comparison, the real and imaginary parts of dielectric permittivity of the ground state are added to the top panel of Fig. 12 marked with a gray solid line. One can observe that when the full laser pulse duration $T = 0.1$ fs, the dielectric permittivity of excited 3C-SiC is consistent with the ground state. As the pulse duration gradually increases to femtosecond order, the change of dielectric permittivity also becomes dramatical. At $T = 0.45$ fs, the dielectric permittivity changes most sharply, which is consistent with the point where 3C-SiC absorbs the most energy as shown in Figs. 3–5. Figure 12 shows that when laser full pulse duration $T = 0.2, 0.45, 0.6,$ and 2.9 fs, the dielectric permittivities along direction either parallel (red solid line, along the x axis) or perpendicular (blue short dashed line, along the z axis) to the polarization direction of the pump single-cycle ultrashort pulse are different, which means that isotropic 3C-SiC is regulated to be an anisotropic material. The peak of optical absorption parallel to the polarization direction of the pump laser pulse is shifted to the red parts of the spectrum (red solid line) and the optical absorption peak in the other direction has a slight blueshift (blue short dashed line) as displayed in Fig. 12(b₄), while

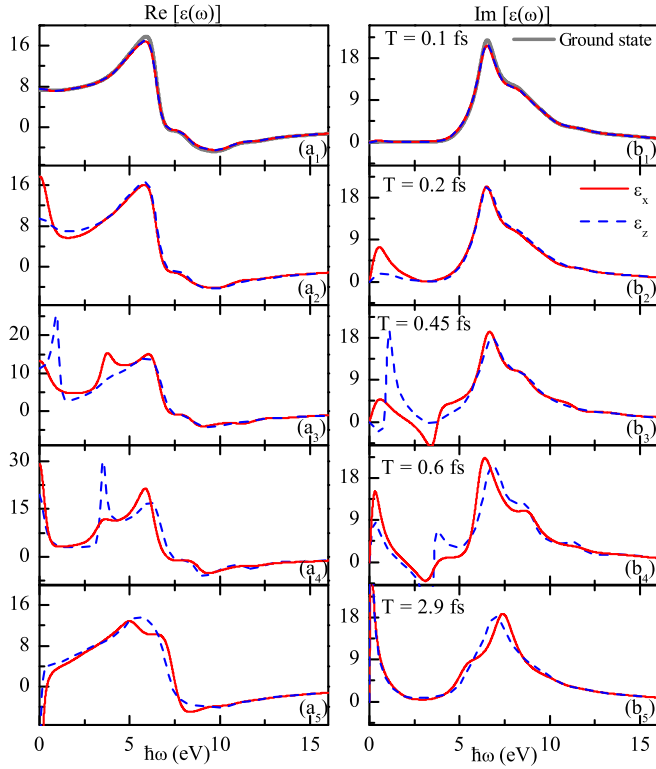


FIG. 12. The real and imaginary parts of dielectric permittivity of excited 3C-SiC induced by the single-cycle ultrashort laser pulses with frequency of $\tau = 0.69$ a.u., $\tau = 1.38$ a.u., $\tau = 3.1$ a.u., $\tau = 4.14$ a.u., and $\tau = 20$ a.u., full duration of 6τ , and peak laser intensity $I = 1 \times 10^{15}$ W/cm². The gray solid lines display the dielectric permittivity in the ground state and excited dielectric permittivity denoted in the direction either parallel (red solid line) or perpendicular (blue short dashed line) to the polarization direction of the pump laser pulses.

with the increase of the full pulse duration to $T = 2.9$ fs, the optical absorption shows a blueshift of the spectrum in both directions, as displayed in Fig. 12(b₅). In the red spectral region, the real parts of dielectric permittivity are negative at low optical frequencies [Fig. 12(a₅)], which is characteristic of metals (strong absorption and negative permittivity at low optical frequencies). This is the metallization effect [69]. This metallization effect manifests itself by a dramatic change in the dielectric properties of the system, which begin to resemble those of metals. In particular, plasmonic phenomena emerge which is also shown in Fig. 13, as discussed later. A stronger low-frequency absorption takes place, which signifies a more developed metallization. The metallization will cause high values of the permittivity and, consequently, bring about the plasmonic behavior of the system. This will open up the field of new dielectric systems with a great deal of new phenomena possible. One potential application is an ultrafast field-effect transistor in which an ultrashort pulse controls a dielectric gate.

As shown in Fig. 12(b₁), 3C-SiC has a stronger absorption around 5–10 eV. Furthermore, as seen in Fig. 8, the longer pulse has a larger component in the range of 5–10 eV. Hence, the longer pulse has more resonant photons for 3C-SiC, resulting in a strong laser-solid interaction. Given the relation of the

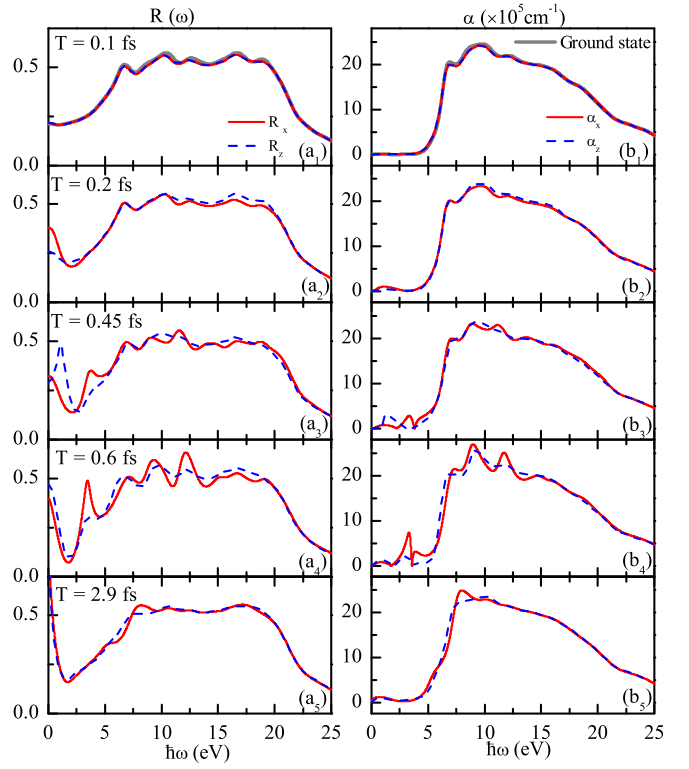


FIG. 13. The reflectivity and absorption coefficient spectrum corresponding to Fig. 12. The gray solid line displays reflectivity and absorption coefficient spectrum in the ground state, reflectivity and absorption coefficient of excited 3C-SiC denoted in the direction either parallel (red solid line) or perpendicular (blue short dashed line) to the polarization direction of the pump laser pulse.

photon energy and the resonance of electronic systems, from the linear response point of view, the closer the absorption peak of solid is to the photon number peak of laser pulse, the stronger the interaction between laser and matter. However, our results show that the laser-matter interaction, including the highest absorption peak (Fig. 3), the most dramatic DOO (Fig. 7), the highest excited electrons number (Fig. 10), and the most obvious electron density difference (Fig. 11), is most obvious when the phase of applied laser field (gray solid lines in Fig. 6) is consistent with the phase of calculated electric current density. This is indeed an uncommon absorption behavior which is different from the traditional linear phenomenon.

As we know, reflectivity and absorption coefficient is a bridge connecting calculated simulation and experiment. The energy-dependent reflectivity $R(\omega)$ can be evaluated by the equation

$$R(\omega) = \left| \frac{\sqrt{\varepsilon_i} - 1}{\sqrt{\varepsilon_i} + 1} \right|^2. \quad (18)$$

The absorption coefficient $\alpha(\omega)$ can be obtained by equation

$$\alpha(\omega) = 2 \frac{\omega \kappa(\omega)}{c}, \quad (19)$$

where $\kappa(\omega)$ is the extinction coefficient, which can be derived from $\varepsilon(\omega)$: $\kappa(\omega) = \sqrt{(|\varepsilon_i| - \text{Re}[\varepsilon_i])/2}$, $i = \parallel$ or \perp , and ε_i is the components of the real parts of dielectric permittivity.

tivity which is parallel or perpendicular to the polarization direction of the pump laser pulse. Figure 13 shows the energy-dependent reflectivity $R(\omega)$ (left panel) and absorption coefficient $\alpha(\omega)$ (right panel) of 3C-SiC irradiated by femtosecond and attosecond laser pulses. R_x (α_x) and R_z (α_z) are the energy-dependent reflectivity (absorption coefficient) that are either parallel or perpendicular to the polarization direction of the pump laser pulse. Under the irradiation of strong ultrashort laser pulses, the energy-dependent reflectivity and absorption coefficient of 3C-SiC would be dramatically modified as the consequence of the high density of carriers generation. The high-density carriers are mainly composed of conduction band electrons whose behavior is like free electrons. The conduction band electrons can change the reflectivity and absorption coefficient by absorbing and reflecting the laser pulse. Besides, the generation of conduction band electrons leads the material to absorb energy through the inverse Bremsstrahlung course, which resulted in the change in dielectric permittivity as shown in Fig. 12. The different manifestations of R_x (α_x) and R_z (α_z) demonstrate that isotropic 3C-SiC has been manipulated to an anisotropic material, similar to the case of dielectric permittivity. The plasmon oscillation frequency ω_p is defined by [70] $\omega_p = \sqrt{\frac{\rho e^2}{m_e \epsilon_0}}$, where ϵ_0 is the permittivity of vacuum. The corresponding electron density is the critical electron density ρ_{cr} and $\rho_{cr} = m_e \epsilon_0 \omega_0^2 / e^2$ when $\omega_p = \omega_0$. When the free carrier density comes up to the plasma frequency equal to the ultrashort laser pulse frequency, the plasma absorption for the laser becomes efficient. According to Drude model, when sufficient electrons in the 3C-SiC crystal are excited, the high excited state surface of 3C-SiC displays the metallic behavior, i.e., high reflectivity and high absorption coefficient, as shown in Fig. 13.

IV. CONCLUSION

In summary, as is well known, it is the electronic state that determines all optical properties of a solid media. A quantitative understanding at the cutting-edge, first-principles theoretical level of how electron dynamics proceed in completely new regimes of intense attosecond pulse light parameters, and in particular of the role of the intense attosecond pulse light, will be critical for applications such as attosecond photonic devices. In this paper, taking 3C-SiC as a concrete example, we theoretically investigate the fundamental strong-field and attosecond response processes in

wide band-gap solids using first-principle approaches by a combination of findings: (i) There is an uncommon response mechanism which we referred to as the linear dynamic interference response mechanism. A typical manifestation of this response mechanism is the energy transfer from intense external light field to matter. Interestingly enough, there are three types of energy transfer in the interaction of solid and attosecond laser pulse, including one resonance case and two nonresonance cases. (ii) The attosecond pulses can effectively manipulate the electric and optical properties of bulk solid materials. The study of the charge transfer controlled by a single-cycle attosecond laser field potentially opens attractive avenues for electron manipulation and growing demands of faster signal processing on the attosecond timescale using wide-band gap dielectric materials, in particular, for the creation of a field-effect transistor controlled by light electric field in the petahertz domain. Using an attosecond pump pulse to dynamically modulate dielectric permittivity of an optical medium offers additional flexibility in controlling the signal light propagation and may open fascinating avenues for all-optical signal processing.

In addition, an important characteristic parameter of the attosecond laser pulse is the duration of its waveform cycle, which is much shorter than the typical carrier scattering time in crystalline solids, therefore, the coherence is maintained greatly during the entire interaction with the attosecond light field. In particular, a coherence transfer from light to materials occurring on the attosecond timescale became critical, leading to the linear dynamic interference response mechanism. As a final note, while on the one hand a good understanding of this type of research is essential since it can provide important insights into the complex light-matter interaction in previously unexplored regimes of parameters where electron correlation, collective effects, and matter characteristics play a key role, on the other hand, this research also could help us to have a detailed understanding of the mechanism of applications in designing devices of attosecond science and technology. Thus, this deserves to be investigated both theoretically and experimentally.

ACKNOWLEDGMENTS

This work was supported by National Natural Science Foundation of China (Grants No. 11774030, No. 11975119, No. 52075004, and No. 51735001), and the Beijing Natural Science Foundation (Grant No. 2192049).

- [1] M. Hentschel, R. Kienberger, C. Spielmann, G. A. Reider, N. Milosevic, T. Brabec, P. Corkum, U. Heinzmann, M. Drescher, and F. Krausz, Attosecond metrology, *Nature (London)* **414**, 509 (2001).
- [2] G. Sansone, E. Benedetti, F. Calegari, C. Vozzi, L. Avaldi, R. Flammini, L. Poletto, P. Villoresi, C. Altucci, R. Velotta *et al.*, Isolated single-cycle attosecond pulses, *Science* **314**, 443 (2006).
- [3] E. Goulielmakis, M. Schultze, M. Hofstetter, V. S. Yakovlev, J. Gagnon, M. Uiberacker, A. L. Aquila, E. Gullikson, D. T.

Attwood, R. Kienberger *et al.*, Single-cycle nonlinear optics, *Science* **320**, 1614 (2008).

- [4] M. J. Abel, T. Pfeifer, P. M. Nagel, W. Boutu, M. J. Bell, C. P. Steiner, D. M. Neumark, and S. R. Leone, Isolated attosecond pulses from ionization gating of high-harmonic emission, *Chem. Phys.* **366**, 9 (2009).
- [5] F. Ferrari, F. Calegari, M. Lucchini, C. Vozzi, S. Stagira, G. Sansone, and M. Nisoli, High-energy isolated attosecond pulses generated by above-saturation few-cycle fields, *Nat. Photon.* **4**, 875 (2010).

- [6] K. Zhao, Q. Zhang, M. Chini, Y. Wu, X. Wang, and Z. Chang, Tailoring a 67 attosecond pulse through advantageous phase-mismatch, *Opt. Lett.* **37**, 3891 (2012).
- [7] F. Frank, C. Arrell, T. Witting, W. Okell, J. McKenna, J. Robinson, C. Haworth, D. Austin, H. Teng, I. Walmsley *et al.*, Invited review article: Technology for attosecond science, *Rev. Sci. Instrum.* **83**, 071101 (2012).
- [8] E. J. Takahashi, P. Lan, O. D. Mücke, Y. Nabekawa, and K. Midorikawa, Attosecond nonlinear optics using gigawatt-scale isolated attosecond pulses, *Nat. Commun.* **4**, 2691 (2013).
- [9] T. Hammond, G. G. Brown, K. T. Kim, D. Villeneuve, and P. Corkum, Attosecond pulses measured from the attosecond lighthouse, *Nat. Photon.* **10**, 171 (2016).
- [10] J. Li, X. Ren, Y. Yin, K. Zhao, A. Chew, Y. Cheng, E. Cunningham, Y. Wang, S. Hu, Y. Wu *et al.*, 53-attosecond x-ray pulses reach the carbon k-edge, *Nat. Commun.* **8**, 1 (2017).
- [11] T. Gaumnitz, A. Jain, Y. Pertot, M. Huppert, I. Jordan, F. Ardana-Lamas, and H. J. Wörner, Streaking of 43-attosecond soft-x-ray pulses generated by a passively CEP-stable mid-infrared driver, *Opt. Express* **25**, 27506 (2017).
- [12] X. Ren, J. Li, Y. Yin, K. Zhao, A. Chew, Y. Wang, S. Hu, Y. Cheng, E. Cunningham, Y. Wu *et al.*, Attosecond light sources in the water window, *J. Opt.* **20**, 023001 (2018).
- [13] Y. X. Zhang, S. Rykovanov, M. Shi, C. L. Zhong, X. T. He, B. Qiao, and M. Zepf, Giant Isolated Attosecond Pulses from Two-Color Laser-Plasma Interactions, *Phys. Rev. Lett.* **124**, 114802 (2020).
- [14] M. Schultze, K. Ramasesha, C. D. Pemmaraju, S. Sato, D. Whitmore, A. Gandman, J. S. Prell, L. J. Borja, D. Prendergast, K. Yabana *et al.*, Attosecond band-gap dynamics in silicon, *Science* **346**, 1348 (2014).
- [15] S. Neppl, R. Ernstorfer, E. M. Bothschafter, A. L. Cavalieri, D. Menzel, J. V. Barth, F. Krausz, R. Kienberger, and P. Feulner, Attosecond Time-Resolved Photoemission from Core and Valence States of Magnesium, *Phys. Rev. Lett.* **109**, 087401 (2012).
- [16] M. Krüger, M. Schenk, and P. Hommelhoff, Attosecond control of electrons emitted from a nanoscale metal tip, *Nature (London)* **475**, 78 (2011).
- [17] A. Borot, A. Malvache, X. Chen, A. Jullien, J.-P. Geindre, P. Audebert, G. Mourou, F. Quéré, and R. Lopez-Martens, Attosecond control of collective electron motion in plasmas, *Nat. Phys.* **8**, 416 (2012).
- [18] A. Wirth, E. Goulielmakis, Z.-H. Loh, R. Santra, N. Rohringer, V. S. Yakovlev, S. Zherebtsov, T. Pfeifer, A. M. Azzeer, M. F. Kling, S. R. Leone, and F. Krausz, Attosecond transient absorption spectroscopy for real-time observation of valence electron motion, in *International Conference on Ultrafast Phenomena* (Optical Society of America, Washington, DC, 2010), p. WE1.
- [19] A. Wirth, M. T. Hassan, I. Grguraš, J. Gagnon, A. Moulet, T. T. Luu, S. Pabst, R. Santra, Z. Alahmed, A. Azzeer *et al.*, Synthesized light transients, *Science* **334**, 195 (2011).
- [20] M. Chini, B. Zhao, H. Wang, Y. Cheng, S. X. Hu, and Z. Chang, Subcycle ac Stark Shift of Helium Excited States Probed with Isolated Attosecond Pulses, *Phys. Rev. Lett.* **109**, 073601 (2012).
- [21] H. Wang, M. Chini, S. Chen, C. H. Zhang, F. He, Y. Cheng, Y. Wu, U. Thumm, and Z. Chang, Attosecond Time-Resolved Autoionization of Argon, *Phys. Rev. Lett.* **105**, 143002 (2010).
- [22] Y. Cheng, M. Chini, X. Wang, A. Gonzalezcastrillo, A. Palacios, L. Argenti, F. Martin, and Z. Chang, Reconstruction of an excited-state molecular wave packet with attosecond transient absorption spectroscopy, *Phys. Rev. A* **94**, 023403 (2016).
- [23] M. Reduzzi, W. Chu, C. Feng, A. Dubrouil, J. Hummert, F. Calegari, F. Frassetto, L. Poletto, O. Kornilov, M. Nisoli *et al.*, Observation of autoionization dynamics and sub-cycle quantum beating in electronic molecular wave packets, *J. Phys. B: At. Mol. Opt. Phys.* **49**, 065102 (2016).
- [24] E. R. Warrick, W. Cao, D. M. Neumark, and S. Leone, Probing the dynamics of Rydberg and valence states of molecular nitrogen with attosecond transient absorption spectroscopy, *J. Phys. Chem. A* **120**, 3165 (2016).
- [25] S. S. Mao, F. Quere, S. Guizard, X. L. Mao, R. E. Russo, G. Petite, and P. Martin, Dynamics of femtosecond laser interactions with dielectrics, *Appl. Phys. A* **79**, 1695 (2004).
- [26] S. Ghimire, A. D. DiChiara, E. Sistrunk, U. B. Szafruga, P. Agostini, L. F. DiMauro, and D. A. Reis, Redshift in the Optical Absorption of ZnO Single Crystals in the Presence of an Intense Midinfrared Laser Field, *Phys. Rev. Lett.* **107**, 167407 (2011).
- [27] K. Leo, Interband optical investigation of Bloch oscillations in semiconductor superlattices, *Semicond. Sci. Technol.* **13**, 249 (1998).
- [28] S. Ghimire, A. Dichiara, E. Sistrunk, P. Agostini, L. F. Dimauro, and D. A. Reis, Observation of high-order harmonic generation in a bulk crystal, *Nat. Phys.* **7**, 138 (2011).
- [29] O. Schubert, M. Hohenleutner, F. Langer, B. Urbanek, C. Lange, U. Huttner, D. Golde, T. Meier, M. Kira, S. W. Koch *et al.*, Sub-cycle control of terahertz high-harmonic generation by dynamical Bloch oscillations, *Nat. Photon.* **8**, 119 (2014).
- [30] A. Schiffrin, T. Paasch-Colberg, N. Karpowicz, V. Apalkov, D. Gerster, S. Mühlbrandt, M. Korbman, J. Reichert, M. Schultze, S. Holzner *et al.*, Optical-field-induced current in dielectrics, *Nature (London)* **493**, 70 (2013).
- [31] M. Durach, A. Rusina, M. F. Kling, and M. I. Stockman, Predicted Ultrafast Dynamic Metallization of Dielectric Nanofilms by Strong Single-Cycle Optical Fields, *Phys. Rev. Lett.* **107**, 086602 (2011).
- [32] E. Goulielmakis, Z. Loh, A. Wirth, R. Santra, N. Rohringer, V. S. Yakovlev, S. Zherebtsov, T. Pfeifer, A. M. Azzeer, M. F. Kling *et al.*, Real-time observation of valence electron motion, *Nature (London)* **466**, 739 (2010).
- [33] F. Krausz and M. Ivanov, Attosecond physics, *Rev. Mod. Phys.* **81**, 163 (2009).
- [34] G. F. Bertsch, J.-I. Iwata, A. Rubio, and K. Yabana, Real-space, real-time method for the dielectric function, *Phys. Rev. B* **62**, 7998 (2000).
- [35] S. Yamada, M. Noda, K. Nobusada, and K. Yabana, Time-dependent density functional theory for interaction of ultrashort light pulse with thin materials, *Phys. Rev. B* **98**, 245147 (2018).
- [36] A. Yamada and K. Yabana, Multiscale time-dependent density functional theory for a unified description of ultrafast dynamics: Pulsed light, electron, and lattice motions in crystalline solids, *Phys. Rev. B* **99**, 245103 (2019).
- [37] N. Troullier and J. L. Martins, Efficient pseudopotentials for plane-wave calculations, *Phys. Rev. B* **43**, 1993 (1991).
- [38] K. Yabana, T. Nakatsukasa, J.-I. Iwata, and G. Bertsch, Real-time, real-space implementation of the linear response time-dependent density-functional theory, *Phys. Status Solidi B* **243**, 1121 (2006).

- [39] T. Otobe, M. Yamagiwa, J.-I. Iwata, K. Yabana, T. Nakatsukasa, and G. F. Bertsch, First-principles electron dynamics simulation for optical breakdown of dielectrics under an intense laser field, *Phys. Rev. B* **77**, 165104 (2008).
- [40] K. Yabana, T. Sugiyama, Y. Shinohara, T. Otobe, and G. F. Bertsch, Time-dependent density functional theory for strong electromagnetic fields in crystalline solids, *Phys. Rev. B* **85**, 045134 (2012).
- [41] F. Kootstra, P. de Boeij, and J. Snijders, Efficient real-space approach to time-dependent density functional theory for the dielectric response of nonmetallic crystals, *J. Chem. Phys.* **112**, 6517 (2000).
- [42] N. T. Maitra, I. Souza, and K. Burke, Current-density functional theory of the response of solids, *Phys. Rev. B* **68**, 045109 (2003).
- [43] G. Wachter, C. Lemell, J. Burgdörfer, S. A. Sato, X.-M. Tong, and K. Yabana, *Ab Initio* Simulation of Electrical Currents Induced by Ultrafast Laser Excitation of Dielectric Materials, *Phys. Rev. Lett.* **113**, 087401 (2014).
- [44] S. A. Sato, K. Yabana, Y. Shinohara, T. Otobe, and G. F. Bertsch, Numerical pump-probe experiments of laser-excited silicon in nonequilibrium phase, *Phys. Rev. B* **89**, 064304 (2014).
- [45] T. Otobe, K. Yabana, and J. Iwata, First-principles calculation of the electron dynamics in crystalline SiO₂, *J. Phys.: Condens. Matter* **21**, 064224 (2009).
- [46] M. A. Marques, A. Castro, G. F. Bertsch, and A. Rubio, octopus: A first-principles tool for excited electron-ion dynamics, *Comput. Phys. Commun.* **151**, 60 (2003).
- [47] A. Castro, H. Appel, M. Oliveira, C. A. Rozzi, X. Andrade, F. Lorenzen, M. Marques, E. Gross, and A. Rubio, basic solid state physics, *Phys. Status Solidi B* **243**, 2465 (2006).
- [48] Web site of OCTOPUS, <http://www.tddft.org/>.
- [49] B. Baumeier, P. Krüger, J. Pollmann, and G. V. Vajenine, Electronic structure of alkali-metal fluorides, oxides, and nitrides: Density-functional calculations including self-interaction corrections, *Phys. Rev. B* **78**, 125111 (2008).
- [50] H. Nakano, K. Watari, Y. Kinemuchi, K. Ishizaki, and K. Urabe, Microstructural characterization of high-thermal-conductivity SiC ceramics, *J. Eur. Ceram. Soc.* **24**, 3685 (2004).
- [51] A. Raffray, R. Jones, G. Aiello, M. Billone, L. Giancarli, H. Golfier, A. Hasegawa, Y. Katoh, A. Kohyama, S. Nishio *et al.*, Design and material issues for high performance SiCf/SiC-based fusion power cores, *Fusion Eng. Design* **55**, 55 (2001).
- [52] R. Verrall, M. Vljajic, and V. Krstic, Silicon carbide as an inert-matrix for a thermal reactor fuel, *J. Nucl. Mater.* **274**, 54 (1999).
- [53] T. Yano, M. Suzuki, H. Miyazaki, and T. Iseki, Effect of neutron irradiation on passive oxidation of silicon carbide, *J. Nucl. Mater.* **233**, 1275 (1996).
- [54] J. P. Perdew, K. Burke, and M. Ernzerhof, Generalized Gradient Approximation Made Simple, *Phys. Rev. Lett.* **77**, 3865 (1996).
- [55] Web site of aflowlib, <http://afLOW.org/search/>.
- [56] S. Sharma, J. K. Dewhurst, A. Sanna, and E. K. U. Gross, Bootstrap Approximation for the Exchange-Correlation Kernel of Time-Dependent Density-Functional Theory, *Phys. Rev. Lett.* **107**, 186401 (2011).
- [57] S. Logothetidis and d. J. Petalas, Dielectric function and reflectivity of 3C-silicon carbide and the component perpendicular to the c axis of 6H-silicon carbide in the energy region 1.5–9.5 eV, *J. Appl. Phys.* **80**, 1768 (1996).
- [58] A. Castro, M. A. Marques, and A. Rubio, Propagators for the time-dependent Kohn-Sham equations, *J. Chem. Phys.* **121**, 3425 (2004).
- [59] K.-M. Lee, C. Min Kim, S. A. Sato, T. Otobe, Y. Shinohara, K. Yabana, and T. Moon Jeong, First-principles simulation of the optical response of bulk and thin-film α -quartz irradiated with an ultrashort intense laser pulse, *J. Appl. Phys.* **115**, 053519 (2014).
- [60] Web site of ELK fp-lapw, <http://elk.sourceforge.net>.
- [61] M. Jiang, S. Peng, H. Zhang, C. Xu, H. Xiao, F. Zhao, Z. Liu, and X. Zu, Ab initio molecular dynamics simulation of the effects of stacking faults on the radiation response of 3C-SiC, *Sci. Rep.* **6**, 20669 (2016).
- [62] P. Földi, M. G. Benedict, and V. S. Yakovlev, The effect of dynamical Bloch oscillations on optical-field-induced current in a wide-gap dielectric, *New J. Phys.* **15**, 063019 (2013).
- [63] V. Apalkov and M. I. Stockman, Metal nanofilm in strong ultrafast optical fields, *Phys. Rev. B* **88**, 245438 (2013).
- [64] M. Noda, S. A. Sato, Y. Hirokawa, M. Uemoto, T. Takeuchi, S. Yamada, A. Yamada, Y. Shinohara, M. Yamaguchi, K. Iida *et al.*, Salmon: Scalable ab-initio light-matter simulator for optics and nanoscience, *Comput. Phys. Commun.* **235**, 356 (2019).
- [65] Web site of SALMON, <https://salmon-tddft.jp/>.
- [66] W.-C. Jiang and J. Burgdörfer, Dynamic interference as signature of atomic stabilization, *Opt. Express* **26**, 19921 (2018).
- [67] W.-C. Jiang, S.-G. Chen, L.-Y. Peng, and J. Burgdörfer, Two-Electron Interference in Strong-Field Ionization of He by a Short Intense Extreme Ultraviolet Laser Pulse, *Phys. Rev. Lett.* **124**, 043203 (2020).
- [68] E. Goulielmakis, V. S. Yakovlev, A. L. Cavalieri, M. Uiberacker, V. Pervak, A. Apolonski, R. Kienberger, U. Kleineberg, and F. Krausz, Attosecond control and measurement: Lightwave electronics, *Science* **317**, 769 (2007).
- [69] M. Durach, A. Rusina, M. F. Kling, and M. I. Stockman, Metallization of Nanofilms in Strong Adiabatic Electric Fields, *Phys. Rev. Lett.* **105**, 086803 (2010).
- [70] L. Jiang and H.-L. Tsai, Energy transport and nanostructuring of dielectrics by femtosecond laser pulse trains, *J. Heat Transfer* **128**, 926 (2006).